Chemical Science

ROYAL SOCIETY OF CHEMISTRY

EDGE ARTICLE

View Article Online
View Journal | View Issue

Cite this: *Chem. Sci.*, 2026, **17**, 1105

All publication charges for this article have been paid for by the Royal Society of Chemistry

Engineering d–p orbital hybridization of single-atom Fe sites *via* axial B-mediation for the oxygen reduction reaction

Xiaoqin Xu,[a] Tianmi Tang,[a] Xue Bai,[a] Tao Gan*[b] and Jingqi Guan *[a]

Single-atom Fe–N–C catalysts have demonstrated promising potential in the oxygen reduction reaction (ORR), yet their intrinsic activity remains less than ideal. Orbital hybridization provides a versatile means to modulate the thermodynamic and kinetic properties during electrochemical processes. In this study, we adopt an "axial ligand boron-modulation" strategy to regulate the electronic structure of single-atom Fe sites through d–p orbital hybridization. The synthesized FeN_4–B/NC demonstrates exceptional ORR activity with a half-wave potential of 0.915 V, surpassing planar FeN_4/NC and commercial Pt/C. *In situ* XAS results reveal the dynamic stretching of Fe–N/O and Fe–B bonds during the ORR process, providing an intuitive confirmation that the single-atom sites undergo reversible structural changes to optimize the adsorption of reaction intermediates. Theoretical investigations combined with zero-field cooling temperature dependence analyses demonstrate that in the intermediate spin state, hybridization occurs between the central Fe's 3d orbitals and B's 2p orbitals, which results in increased e_g orbital occupancy and positions the d-band center closer to the Fermi level, which enhances charge transfer efficiency and O_2 adsorption capabilities. Furthermore, the newly developed FeN_4–B/NC catalyst shows remarkable performance in liquid and quasi-solid-state zinc–air batteries.

Received 13th September 2025
Accepted 12th November 2025

DOI: 10.1039/d5sc07064c

rsc.li/chemical-science

Introduction

With the advancement of flexible and wearable electronic devices, zinc–air batteries (ZABs) with high energy density, low cost, and safety demonstrate significant potential for practical applications.[1,2] The oxygen reduction reaction (ORR) plays a pivotal role in ZAB systems. Although platinum-based catalysts are widely regarded as the optimal choice for the ORR due to their exceptional catalytic activity, the prohibitively expensive nature, scarce resources, limited stability, and poor tolerance to CO/methanol significantly hinder their large-scale implementation.[3] Therefore, it is highly desirable to explore low-cost, non-precious metal-based catalysts with remarkable catalytic performance.

Single-atom catalysts (SACs), characterized by their atomically dispersed metal active sites, represent promising experimental and theoretical models for elucidating catalytic mechanisms and guiding the rational design of ORR catalysts.[4] This is attributed to their high metal atom efficiency, unique electronic structure, and uniformly tunable active sites.[5,6] In this regard, Fe-based catalysts with square-planar Fe–N_4 centers are widely regarded as promising candidates for achieving high-efficiency ORR activity and replacing Pt-based catalysts.[7,8] However, the strong binding affinity of Fe–N_4 centers towards *OH intermediates hinders the desorption of OH^- or H_2O, thereby limiting their catalytic activity and kinetics.[9,10] Recent studies have demonstrated that the incorporation of foreign atoms at the fifth coordination position, such as Cl,[11,12] O,[13] S,[10] or I,[14] can regulate the electronic properties of Fe-based active sites. This modulation occurs because the Fe–O bonds formed between ORR intermediates and Fe–N_4 sites involve axial orbital overlap relative to the Fe–N_4 plane, thereby significantly improving the ORR performance.[15] In addition, Fe, as a transition metal with localized d orbitals, exhibits the unique ability to engage in d–p orbital hybridization with heteroatoms that possess p orbitals. Through this d–p orbital hybridization, Fe improves its charge transfer capabilities by modifying the electronic environment and optimizing the energy levels of relevant orbitals. This enhancement facilitates more efficient participation of electrons in electrochemical reactions.[16] However, due to the ionic nature of their axial ligands binding to Fe–N_4 sites, such ligands tend to leach during the ORR process.[17] Establishing stable charge distribution at Fe–N_4 sites is therefore fundamentally and practically significant. If such stability can be achieved, it would pave the way for progressive enhancement in the ORR activity of Fe–N_4 SACs.

Here, we introduce a novel d–p orbital hybridization approach facilitated by the axial coordination of B to enhance the intrinsic ORR activity. Utilizing a molecular-cage

[a]*Institute of Physical Chemistry, College of Chemistry, Jilin University, Changchun 130021, PR China. E-mail: guanjq@jlu.edu.cn*

[b]*Shanghai Synchrotron Radiation Facility, Shanghai Advanced Research Institute, Chinese Academy of Sciences, Shanghai, PR China. E-mail: gant@sari.ac.cn*

encapsulation approach combined with ligation strategies, we synthesized two Fe SACs with distinct active centers on N-doped carbon supports, including square-planar FeN_4 and quasi-octahedral geometry FeN_4–B configurations. Notably, the FeN_4–B catalyst demonstrated superior ORR performance in alkaline media, significantly outperforming FeN_4-based catalysts. Density functional theory (DFT) calculations revealed that the interactions between B's 2p orbitals and Fe's 3d orbitals (d_{z^2}, d_{xz}, and d_{yz}) establish both bonding and antibonding interactions. This orbital coupling induces an upshift of the d-band center, which facilitates *OH adsorption and consequently reduces the energy barrier for the rate-determining step (RDS) of the ORR. To further evaluate the practical application potential of FeN_4–B, we incorporated it as the cathode in a ZAB system with a solid-state configuration. The FeN_4–B/NC-based ZAB exhibited exceptional performance, delivering higher power density and energy density compared to the commercial Pt/C + RuO_2-based ZAB, demonstrating its immense potential for practical applications.

Results and discussion

Structure and composition analyses

The synthesis procedure for the carbon nanocage catalyst incorporating single-atom FeN_4–B sites is illustrated in Fig. 1a. To construct FeN_4–B/NC, we employed a molecular cage encapsulation strategy. Iron(II) phthalocyanine (Fe Pc), which possesses a condensed aromatic ring framework and well-defined molecular structure, was utilized as the metal precursor. 5-Borondiphenic acid (5-bop) served as the boron source. The synthesis proceeded through three key steps. First, Fe Pc and 5-bop underwent Lewis acid–base interactions to form Fe Pc@5-bop complexes (10.3 Å × 7.6 Å). These complexes were then immersed in a methanol solution containing Zn^{2+} ions and 2-methylimidazole to encapsulate them within ZIF-8 nanocages (11.6 Å). Finally, high-temperature annealing was conducted to obtain the final FeN_4–B/NC material.

It was observed *via* scanning electron microscopy (SEM) in Fig. S1 that the annealed FeN_4–B/NC exhibited a consistent morphology with Fe Pc@5-bop@ZIF-8, indicating that no collapse occurred during the process. Transmission electron microscopy (TEM), high-angle annular dark-field scanning transmission electron microscopy (HAADF-STEM) and energy-dispersive X-ray spectroscopy (EDS) mapping of Fe Pc@5-bop@ZIF-8 show that Fe Pc@5-bop is encapsulated in ZIF-8 and the dodecahedral appearance of ZIF-8 is not compromised, and Fe and B are uniformly distributed in ZIF-8 (Fig. S2). TEM reveals that FeN_4–B/NC retains the regular rhombic dodecahedral structure of ZIF-8 (Fig. 1b). No clusters or nanoparticles were observed in the high resolution-TEM (HR-TEM) image (Fig. 1c), while clear lattice fringes corresponding to graphitized carbon structures were evident. The HAADF-STEM image of the sample does not show visible iron-based nanoparticles (Fig. 1d). EDS mapping (Fig. 1e) demonstrates uniform distribution of Fe, C, N, and B elements within the FeN_4–B/NC polyhedral framework. The face-scanning analysis using HAADF-STEM combined with EDS shows that the elemental content of Fe in the FeN_4–B/NC catalyst is 0.49 wt% (Fig. S3). This further indicates that the encapsulation–thermal decomposition strategy successfully anchored the atomically dispersed Fe sites in the carbon substrate and achieved a considerable active site density. Aberration-corrected (AC) HAADF-STEM imaging allows atomic-level observation of the FeN_4–B/NC structure (Fig. 1f). Numerous isolated points are identified, which correspond to iron atoms as clearly visualized in the corresponding 3D representation (Fig. 1g).

X-ray diffraction (XRD) patterns of Fe Pc@ZIF-8 and Fe Pc@5-bop@ZIF-8 are consistent with those of ZIF-8, indicating that the incorporation of Fe Pc and Fe Pc@5-bop does not disrupt the structural integrity of ZIF-8 (Fig. S4a). Furthermore, no Fe metal signals were detected in the XRD patterns of these samples after thermal decomposition (Fig. S4b). Additionally, the graphitic characteristics of the catalysts were systematically investigated using Raman spectroscopy to evaluate their degree of graphitization. In the Raman spectra, the D peak corresponds to defects while the G peak represents the graphitization degree. As shown in Fig. S5, the FeN_4–B/NC sample exhibits a lower I_D/I_G ratio (1.01), indicating a higher degree of graphitization and consequently enhanced electrical conductivity.

To investigate the chemical states of FeN_4–B/NC and FeN_4/NC, X-ray photoelectron spectroscopy (XPS) analysis was conducted. The survey spectra reveal the presence of C, N, O, and Fe elements in both samples (Fig. S6a). Additionally, a distinct B peak was observed for FeN_4–B/NC, confirming the successful incorporation of B atoms within the carbon nanocage framework. As shown in Fig. S6b, the high-resolution C 1s XPS spectrum was deconvoluted into three characteristic peaks: C–C (284.8 eV), C–N (285.6 eV), and O–C=O (286.9 eV).[18] The Fe 2p spectra for both samples are shown in Fig. 2a. The Fe 2p spectra exhibit four prominent peaks at binding energies of 708.4 eV (Fe^{2+} $2p_{3/2}$), 714.7 eV (Fe^{3+} $2p_{3/2}$), 722.9 eV (Fe^{2+} $2p_{1/2}$), and 726.9 eV (Fe^{3+} $2p_{1/2}$).[19] Relative to FeN_4/NC, the binding energy shifts of both the Fe $2p_{1/2}$ and $2p_{3/2}$ orbitals in FeN_4–B/NC exhibited higher values. This observation suggests an electron transfer from Fe to B, accompanied by an increase in electron density around the Fe center.[20] As shown in Fig. 2b, the B 1s XPS spectrum of FeN_4–B/NC reveals four distinct boron species: Fe–B (~190.3 eV), B–C (~190.9 eV), B–N (~191.8 eV), and B–O (~193.1 eV).[21] The presence of the Fe–B bond provides direct evidence of chemical bonding between boron and iron, ruling out the possibility of mere π–π stacking interactions. Based on the N 1s spectroscopy analysis (Fig. 2c), both FeN_4–B/NC and FeN_4/NC samples exhibit pyridinic N (398.4 eV), Fe–N (399.5 eV), pyrrolic N (400.9 eV), graphitic N (402.5 eV), and oxidized N (404.7 eV) species.[22] However, significant differences in their nitrogen coordination environments are observed: FeN_4/NC predominantly features pyrrolic N, whereas FeN_4–B/NC shows a preference for pyridinic N. This indicates that FeN_4/NC adopts a wrinkled structure, while FeN_4–B/NC exhibits a planar tetragonal FeN_4 coordination geometry.[23] The structural modification arises from the incorporation of B, which strengthens the Fe–N interaction and facilitates the conversion of pyrrolic N to more stable pyridinic N and modulates the FeN_4–B/NC's electronic properties and optimizes the distribution of active

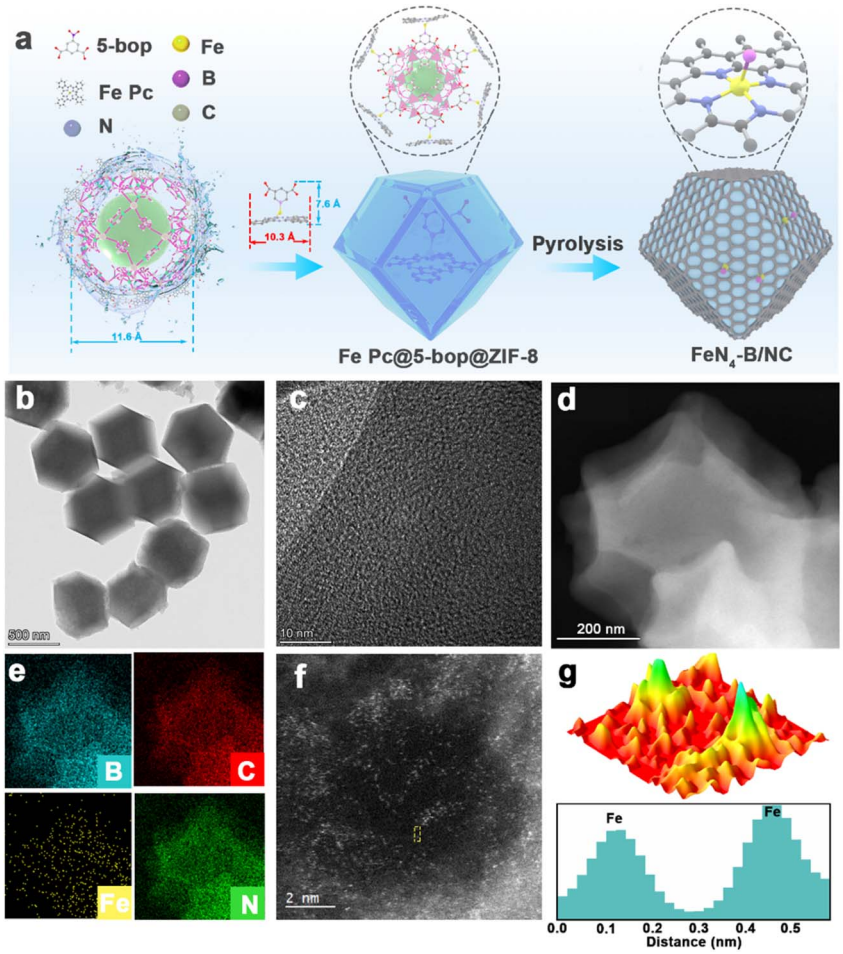

Fig. 1 (a) Illustration of the synthetic pathway for FeN_4–B/NC. (b) TEM image, (c) HR-TEM image and (d) HAADF-STEM image of FeN_4–B/NC. (e) Elemental mapping images showing the distribution of Fe, C, N, and B. (f) AC-STEM image and (g) three-dimensional atomic overlap maps and intensity profile derived from the Gaussian function fitting of the yellow box in (f).

sites. This structural optimization ultimately enhances both catalytic performance and operational durability.[24,25]

To probe the intricate details of local coordination geometry and electronic states, X-ray absorption near-edge structure (XANES) and extended X-ray absorption fine structure (EXAFS) spectroscopic analyses were employed. As shown in Fig. 2d, the absorption edge of Fe in FeN_4–B/NC is positioned between those of FeO and Fe_2O_3, indicating that the average oxidation state of Fe is between +2 and +3.[26] Compared to FeN_4/NC, a noticeable positive shift in the Fe K-edge suggests a change in the electronic structure of Fe sites, which means an increase in the oxidation state of Fe. This is likely due to the B axial coordination leading to electron transfer from Fe to B,[27] consistent with previous XPS observations.[11] In the inset of Fig. 2d, after B incorporation, the intensity of the pre-edge peak decreases (related to the 1s–4p_z dipolar transition in a planar D_{4h} configuration), indicating that the local symmetry transitions from planar D_{4h} to C_{4v}.[28,29] Fourier-transformed k^3-weighted EXAFS spectra were plotted. As shown in Fig. 2e, FeN_4 exhibits a prominent peak centered at 1.63 Å in the *R*-space, corresponding to the Fe–N scattering path. Notably, a shoulder peak at 2.1 Å is observed for FeN_4–B/NC, which corresponds to Fe–B backscattering, further confirming the presence of an Fe–B axial interaction.[30] The absence of Fe–Fe features in FeN_4–B/NC and FeN_4/NC samples indicates that Fe sites are atomically dispersed within the carbon framework. To elucidate the coordination environment around Fe sites, quantitative least-squares EXAFS curve fitting was performed. In the FeN_4/NC structure, iron centers are each bonded to four nitrogen atoms in the first coordination shell, with a mean bond distance of 1.92 Å (Fig. 2f and Table S3). In contrast, Fe in FeN_4–B/NC is bonded to four N atoms and one B atom (FeN_4–B), with an average bond length of 1.96 Å and 2.15 Å, respectively (Fig. 2g). Importantly, the FT k^3-weighted EXAFS spectra match perfectly with the simulated EXAFS spectra obtained from DFT, further validating the proposed FeN_4–B structure. Additionally, in the wavelet transform (WT)-EXAFS plots, we observe minor peak shifts in the *k*-space between FeN_4/NC and FeN_4–B/NC (Fig. 2h), indicating subtle changes in their atomic coordination environments.[21]

Electrochemical performances

The ORR electrocatalytic performance was evaluated using a rotating disk electrode (RDE) in an O_2-saturated 0.1 M KOH

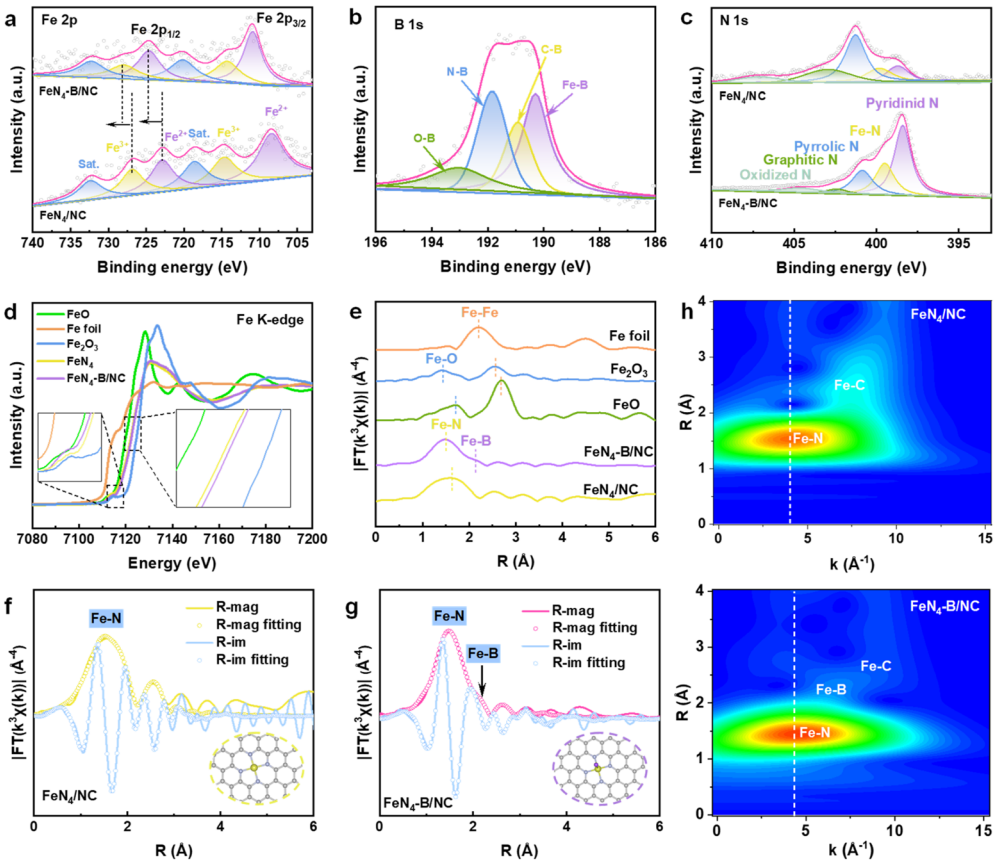

Fig. 2 XPS spectra of (a) Fe 2p, (b) B 1s, and (c) N 1s. (d) Fe k-edge XANES spectra. (e) FT-EXAFS spectra for (d) Fe k-edge. FT-EXAFS of the *R*-space fitting curve for (f) FeN_4/NC and (g) FeN_4–B/NC (inset: model of FeN_4 and FeN_4–B). (h) WT-EXAFS plots.

solution. As shown by the comparative cyclic voltammetry (CV) curves, all synthesized catalysts exhibit distinct reduction peaks (Fig. 3a).[31] Notably, FeN_4–B/NC achieves the most positive peak potential, indicating its potentially superior ORR activity. Linear scan voltammetry (LSV) curves (Fig. 3b) reveal that FeN_4–B/NC delivers an outstanding half-wave potential ($E_{1/2}$) of 0.915 V *vs.* RHE, surpassing those of FeN_4/NC (0.866 V), NC (0.748 V), and commercial Pt/C (0.850 V). This improvement demonstrates that the B-axial coordination in FeN_4 configuration enhances the ORR performance through synergistic electronic modulation. Furthermore, as shown in Fig. 3c, the Tafel slope of FeN_4–B/NC (44 mV dec^{-1}) is significantly lower than those of FeN_4/NC, NC, and Pt/C, suggesting that the incorporation of B-axial coordination at the Fe site effectively accelerates ORR kinetics. Fitting the LSV curves at various rotation speeds with the K–L equation reveals that the electron transfer number of FeN_4–B/NC is approximately 4.0, indicating a 4-electron ORR process (Fig. 3d and S7). RRDE tests further demonstrate that FeN_4–B/NC exhibits a higher electron transfer number closer to 4 than FeN_4/NC. The introduction of axial B-coordination reduces the H_2O_2 yield from 11% to 1%, suggesting enhanced O_2 dissociation and superior ORR activity for FeN_4–B/NC (Fig. 3e). Furthermore, the turnover frequency (TOF) of FeN_4–B/NC at 0.8 V is 0.982 O_2 s^{-1}, which is much higher than that of Pt/C (0.049 O_2 s^{-1}), indicating that the iron-related active sites in FeN_4–B/NC have high efficiency in the ORR.[32]

In addition to its excellent ORR activity, stability of a catalyst is crucial for practical applications. The long-term durability of FeN_4–B/NC for the ORR was evaluated using chronoamperometric measurements. Notably, FeN_4–B/NC shows a minimal current decay of only 5.8% over 11 hours of continuous operation, significantly outperforming Pt/C, which exhibits an 11.4% current loss (Fig. 3f). Furthermore, in methanol tolerance tests conducted after 200 seconds of potentiostatic measurement (Fig. 3g), commercial Pt/C displays severe current fluctuations and a noticeable drop upon addition of 1 mL methanol, whereas FeN_4–B/NC maintains relatively stable current responses, demonstrating strong resistance to methanol poisoning.[33] Compared to other SACs reported previously, FeN_4–B/NC achieves top-tier activity (Fig. 3h and Table S3). The accelerated durability test (ADT) results reveal that after 5000 cycles of testing, the half-wave potential in alkaline electrolyte decreases by 22 mV for FeN_4–B/NC, whereas a more significant loss of 38 mV is observed for Pt/C (Fig. S8). These findings demonstrate the superior stability of FeN_4–B/NC during the ORR. We further evaluated the oxygen evolution reaction (OER) performance of FeN_4–B/NC in 1 M KOH solution. As shown in Fig. S9, the FeN_4–B/NC exhibited an overpotential of 370 mV at

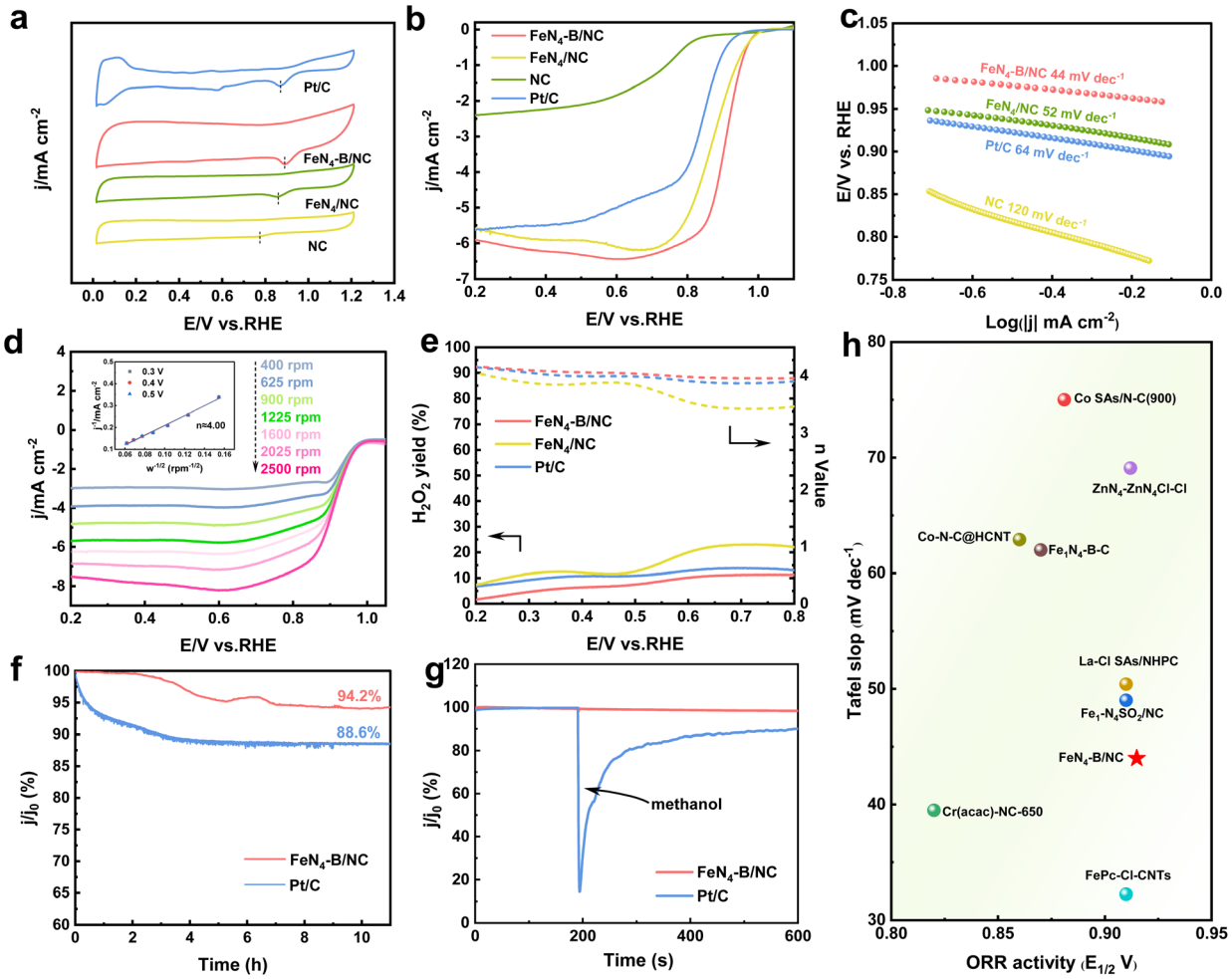

Fig. 3 (a) CV plots. (b) LSV curves. (c) Tafel plots. (d) The polarization curves at different rotation speeds and the corresponding K–L plots (shown as inset) for FeN_4–B/NC. (e) H_2O_2 yields and the corresponding *n*. Chronoamperometric (*i*–*t*) responses of (f) before and (g) after the addition of 1 mL of methanol. (h) Comparative analysis of the ORR performance of FeN_4–B/NC against contemporary SACs and SACs with axial coordination.

a current density of 10 mA cm^{-2}, comparable to that of RuO_2 and superior to that of FeN_4/NC (380 mV).[34]

Study on the oxygen electrocatalysis mechanisms

To investigate the structural evolution of FeN_4–B/NC during the ORR process, *in situ* XAS experiments were conducted. The XAS spectra of FeN_4–B/NC were collected at different potentials in O_2-saturated 0.1 M KOH solution. As shown in Fig. 4a, a negative shift in the absorption edge energy was observed with decreasing applied potential, providing evidence for the occurrence of the ORR.[35] To further probe the structural changes at the active sites during the ORR, EXAFS oscillations were analyzed. The Fe K-edge FT-EXAFS spectra (Fig. 4b) reveal the structural stability of FeN_4–B/NC to retain its initial structural integrity under operating conditions. Specifically, as the applied voltage decreases, the Fe–N/O bond length shortens from 1.52 to 1.39 Å, while the Fe–B bond length extends from 2.11 to 2.21 Å, demonstrating that at different potentials, both Fe–N/O and Fe–B bonds undergo stretching due to intermediate adsorption at the active centers.[36] Additionally, variations in the intensities of Fe–N/O and Fe–B bonds were observed at different potentials, likely attributed to redox processes involving Fe atoms and structural rearrangements. These changes were further influenced by the adsorption and desorption of reaction intermediates, suggesting dynamic structural modifications of FeN_4–B during the ORR. The FT-EXAFS fitting results at various potentials showed an increase in the coordination number of Fe–N/O bonds (Fig. 4c–f and Table S2), indicating that Fe atoms serve as the active centers for the ORR. Furthermore, Fig. S10 displays the WT plots of FeN_4–B/NC at different potentials, showing partial shifts in Fe–N/O scattering paths, which further confirms that Fe atoms are the active sites for the ORR.

Theoretical calculations revealed that the axial coordination of B to FeN_4 significantly influences both the electronic structure and ORR performance. The optimized structures of FeN_4 and FeN_4–B are presented in Fig. 5a. It can be seen that establishing the axial coordination of B at the Fe–N_4 locus causes the distortion of the square-plane field around Fe–N_4, which is transformed into a quasi-octahedral geometry. Bader charge

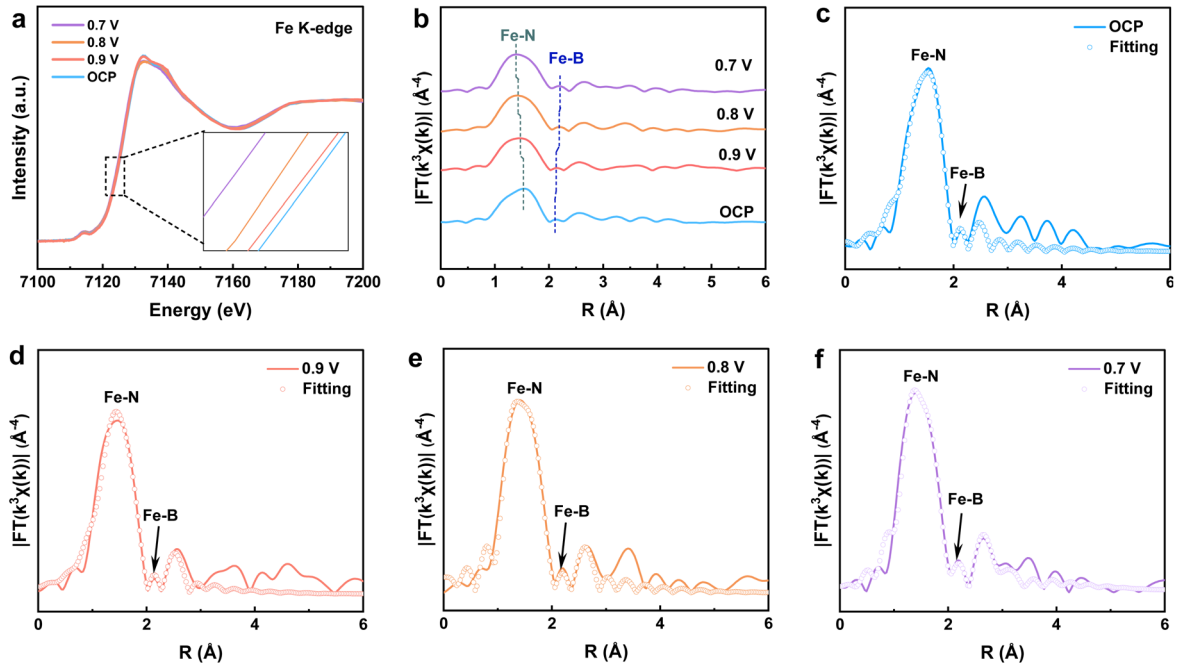

Fig. 4 (a) *In situ* XANES of the Fe k-edge of FeN_4–B/NC at various potentials. (b) FT-EXAFS spectra of the Fe k-edge at various potentials. (c–f) Fe k-edge FT-EXAFS of the *R*-space fitting curve at OCP, 0.9, 0.8 and 0.7 V, respectively.

analysis reveals the net charge on individual atoms, where positive values indicate electron loss (oxidation) and negative values reflect electron gain (reduction).[37] As evidenced by the calculations (Fig. 5a), the Bader charges for Fe in FeN_4 and FeN_4–B systems are determined to be −1.39 and −0.93, respectively. This suggests an electronic transfer from Fe to B, leading to an increase in Fe's valence state in agreement with the aforementioned XPS and XAS results.[38] As shown by differential charge density plots (Fig. 5b–d), electron transfer in symmetric FeN_4 occurs exclusively within the FeN_4 plane, with a symmetrical distribution of electron clouds. In contrast, the axial B atom in FeN_4–B interacts with the Fe metal center, inducing pronounced charge redistribution in the axial region and breaking the symmetry of charge distribution within the FeN_4 plane. Free energy diagrams for the ORR on both catalysts are plotted in Fig. S11 and S12. At $U = 0$ V (Fig. 5e), the RDS of FeN_4–B exhibits a higher energy barrier ($\Delta G = -0.84$ eV) compared to FeN_4 ($\Delta G = -0.61$ eV). Conversely, at $U = 1.23$ V (Fig. 5e), the ΔG for the rate-determining step in FeN_4 (−0.64 eV) is significantly higher than that of FeN_4–B (−0.24 eV).[39] These results indicate that introducing axially coordinated B atoms at the FeN_4 site can effectively reduce the energy barrier, thereby enhancing the intrinsic ORR activity.[40] Moreover, FeN_4–B shows a lower initial oxygen activation energy barrier compared to FeN_4, indicating enhanced oxygen adsorption capability.

As revealed by the density of states (DOS) analysis (Fig. 5f and g), the incorporation of an axial B atom causes a shift in the d-band center from −0.98 eV for the FeN_4 to −0.67 eV for the FeN_4–B.[41] The elevation of the d-band center facilitates electron excitation to anti-bonding orbitals, increasing their occupation and thereby enhancing the O_2 adsorption capability at the Fe site.[42,43] This upward shift is attributed to the increased occupancy of e_g orbitals due to the introduction of a high-energy p-band, leading to enhanced unpaired electrons, which facilitate charge transfer and improve reaction kinetics.[44] To investigate the spin states of FeN_4–B/NC, we employed zero-field-cooled temperature-dependent (ZFC-T) magnetic susceptibility (χ_m) measurements. Through analysis of the temperature-dependent χ^{-1} data (Fig. 5h), we determined that FeN_4–B exhibits an effective magnetic moment of 2.83 μB, with a $t_{2g}^4e_g^1$ electron configuration, revealing a middle-spin state (M.S.).[45] The d-orbitals split into four distinct states: $d_{x^2-y^2}$, d_{xy}, and two-fold degenerate d_{xz}/d_{yz}. The d_{z^2} and d_{xz}/d_{yz} orbitals undergo hybridization with the p orbitals of B atoms, resulting in bonding (σ and π) and antibonding (σ* and π*) states.[46] In contrast, the horizontal d-orbitals ($d_{x^2-y^2}$ and d_{xy}) remain non-binding due to their inactivity.[47] As shown in Fig. 5i, the projected density of states (PDOS) analysis reveals a strong orbital overlap between Fe 3d ($d_{z^2}/d_{xz}/d_{yz}$) and B 2p orbitals in FeN_4–B, indicating a significant d–p coupling effect that generates both bonding (σ and π) and antibonding (σ* and π*) states (Fig. 5i).[48,49] Based on the orbital hybridization theory and the observed PDOS overlap, we determine the optimal electron occupancy across these bonding and antibonding states.[50] As illustrated in Fig. 5j, the vacant $2p_z$ orbital of B^- can accept an electron from the $3d_{z^2}$ orbital of middle-spin Fe^{3+}.[51] This process involves the delocalization of electrons into σ orbitals, thereby preventing excessive occupancy of the antibonding σ* orbital and facilitating the reaction progress.[52] Additionally, the half-filled $2p_x$ and $2p_y$ orbitals of B^- enable moderate π* coupling with the $3d_{xz}$ and $3d_{yz}$ orbitals of Fe^{3+}.[53,54] This coupling stabilizes the Fe sites without fully occupying the d-electrons, thus optimizing the adsorption energies for *OOH and *OH species.[55]

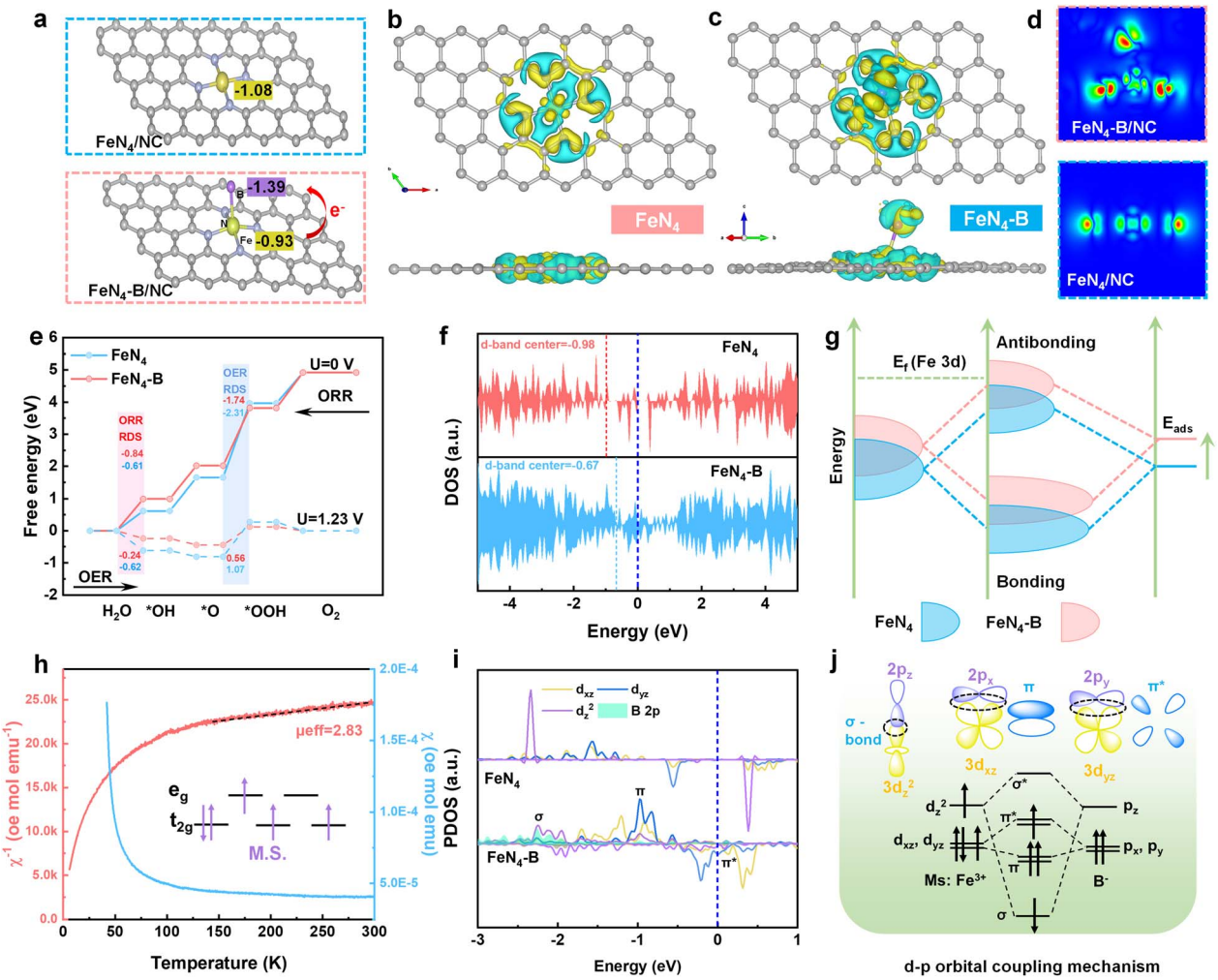

Fig. 5 (a) Optimization model and Bader charge of FeN_4 and FeN_4–B. Electron density difference maps of (b) FeN_4 and (c) FeN_4–B. (d) 2D slice of differential charge. Yellow and blue regions indicate areas of increased and decreased electron density, respectively. The free energy step diagram at (e) $U = 0$ V and $U = 1.23$ V. (f) DOS. (g) Schematic of bonding status and adsorption behavior under FeN_4 (blue) and FeN_4–B (red). (h) χ–T plots and χ^{-1}–T plots. (i) PDOS of FeN_4 and FeN_4–B. (j) The orbital interaction between Fe and B.

Application of FeN_4–B/NC in ZABs

Motivated by the remarkable ORR and OER performance of FeN_4–B/NC, liquid and flexible ZABs were developed by utilizing FeN_4–B/NC as the air cathode and Zn foil as the anode (Fig. 6a). As illustrated in Fig. 6b, the ZAB utilizing FeN_4–B/NC as the cathode demonstrates an open-circuit voltage (OCV) of 1.504 V, which exceeds that of the ZAB with a Pt/C + RuO_2 cathode (1.450 V) within a 50-minute period. This reduction is attributed to the enhanced charge and discharge capabilities of FeN_4–B/NC. Furthermore, the FeN_4–B/NC-based ZAB achieves a maximum power density of 186 mW cm^{-2} (Fig. 6c), which considerably surpasses that of the commercial Pt/C + RuO_2-based ZAB (52 mW cm^{-2}). The FeN_4–B/NC-based ZAB demonstrates a remarkable specific capacity of 790 mAh g_{Zn}^{-1}, which not only meets the required standards, but also surpasses that of Pt/C + RuO_2-based ZAB (744 mAh g_{Zn}^{-1}) (Fig. 6d). The FeN_4–B/NC-based ZAB demonstrates minimal decline in discharge/charge performance over 300-hour of cycling at 10 mA cm^{-2}, with a 10-minute discharge and 10-minute charge process. In contrast, the Pt/C + RuO_2-based ZAB experiences significant degradation within 65 hours, further validating the superior ORR/OER stability of the FeN_4–B/NC-based cathode (Fig. 6e). In addition, the FeN_4–B/NC-based ZAB demonstrates a notable and consistent round-trip efficiency, increasing from an initial 58.3% to a final 61.1%, highlighting its exceptional recharging performance (inset of Fig. 6e). According to Fig. 6f, the discharge voltages of FeN_4–B/NC-based batteries at current densities of 5, 10, 25, and 50 mA cm^{-2} are 1.24, 1.20, 1.12, and 1.02 V, respectively. The outstanding stability of the FeN_4–B/NC catalyst is the result of the inherent rigidity of the FeN_4 structure, the additional stability provided by the axial B ligands, the efficient charge transfer ability, and the ideal adsorption strength ensured by the resulting intermediate spin state, all of which work together in synergy. Even after the current density is returned to 5 mA cm^{-2}, the system sustains a stable discharge voltage of 1.24 V, highlighting its remarkable rate performance. Compared with

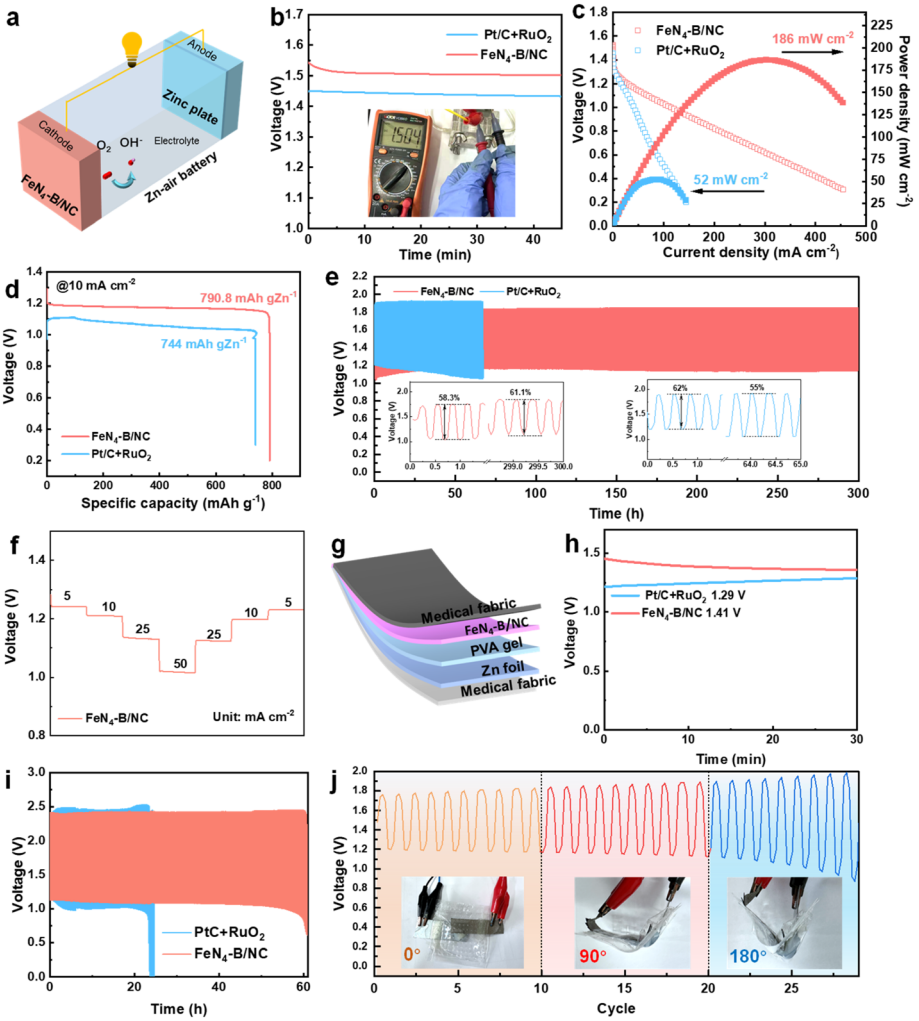

Fig. 6 (a) Schematic illustration of the self-assembly process of a ZAB with FeN_4-B/NC as air cathode. (b) OCV plots (inset: OCV recorded by a multimeter). (c) Polarization curve for discharge and corresponding power density. (d) Specific capacity at 10 mA cm^{-2}. (e) Charge–discharge cycling performance at 10 mA cm^{-2}. (f) Discharge curves under different current densities. (g) Schematic diagram of the homemade FZAB. (h) OCV plots. (i) Cycling tests of the FZAB with the FeN_4-B/NC cathode and (j) under various bending degrees.

other Fe SACs, the FeN_4–B/NC-based ZABs exhibit superior performance and stability as evidenced in Table S4.

To explore the feasibility of the FeN_4–B/NC electrocatalyst in flexible and wearable electronics, an all-solid-state flexible ZAB (FZAB) was assembled, as shown in Fig. 6g. To simplify the testing procedure, we assembled a sandwich-type FZAB using a piece of zinc foil, an electrolyte membrane with a hydrogel, and a cathode with FeN_4–B/NC through a layer-by-layer method. The flexible ZAB with the FeN_4–B/NC cathode achieves a stable OCV of ~1.41 V, surpassing the performance of the Pt/C + RuO_2-based counterpart (Fig. 6h). Furthermore, the cycling stability of the FeN_4–B based FZAB reached 62 hours at a current density of 2 mA cm^{-2} and a charge–discharge rate of 4 min per cycle (Fig. 6i), which exceeded that of the Pt/C based FZAB (26 hours). The FeN_4–B/NC-based flexible ZAB exhibited stable charge/discharge voltages at various bending states (0°, 90° and 180°), further demonstrating the practical application potential of the FeN_4–B/NC cathode (Fig. 6j).[56]

Conclusions

In summary, a "B-mediation" strategy has been developed to transform planar FeN_4 into a pseudo-octahedral FeN_4–B configuration, where an axial B atom coordinates with the FeN_4 center. This approach modulates the electronic structure of Fe single atoms through d–p orbital hybridization, achieving an ORR half-wave potential of 0.915 V for FeN_4–B/NC and an OER overpotential of 370 mV at 10 mA cm^{-2}. *In situ* XAS confirmed the dynamic structural changes of the Fe sites during the reaction process, providing direct evidence for its outstanding performance. DFT calculations revealed that d–p orbital hybridization between the axial B atom and Fe centers shifts the d-band center closer to the Fermi level and optimizes *OH intermediate adsorption, thereby reducing the reaction energy barrier for the RDS and facilitating both ORR and OER processes. Experimental validation using a liquid ZAB setup demonstrated the practical potential of FeN_4–B/NC, delivering

remarkable power density and capacity (186 mW cm^{-2} and 790.8 mAh g_{Zn}^{-1}, respectively), along with robust stability over 300 hours of operation. Furthermore, FeN_4–B/NC showed promise for flexible ZABs with an open-circuit voltage of 1.41 V and stable charge–discharge cycling performance under various bending angles.

Author contributions

All of the authors contributed to the literature search, writing and editing of this review.

Conflicts of interest

There are no conflicts to declare.

Data availability

The data supporting this article have been included as part of the supplementary information (SI). Supplementary information: experimental methods, electrochemical evaluation, Zn–air battery test, DFT methods, Fig. S1–S12 and Tables S1–S4. See DOI: https://doi.org/10.1039/d5sc07064c.

Acknowledgements

This work was supported by the National Natural Science Foundation of China (No. 22075099), and the Education Department of Jilin Province (No. JJKH20250070BS). The authors acknowledge the BL11B beamline (31124.02.SSRF.BL11B) of the Shanghai Synchrotron Radiation Facility for providing the XAS beamtime.

Notes and references

1 Y. Wang, J. Wu, S. Tang, J. Yang, C. Ye, J. Chen, Y. Lei and D. Wang, Synergistic Fe–Se atom pairs as bifunctional oxygen electrocatalysts boost low-temperature rechargeable zn–air battery, *Angew. Chem., Int. Ed.*, 2023, **62**, e202219191.

2 T. Tang, W.-J. Jiang, X.-Z. Liu, J. Deng, S. Niu, B. Wang, S.-F. Jin, Q. Zhang, L. Gu, J.-S. Hu and L.-J. Wan, Metastable rock salt oxide-mediated synthesis of high-density dual-protected M@NC for long-life rechargeable zinc–air batteries with record power density, *J. Am. Chem. Soc.*, 2020, **142**, 7116–7127.

3 J. Fu, R. Liang, G. Liu, A. Yu, Z. Bai, L. Yang and Z. Chen, Recent progress in electrically rechargeable zinc–air batteries, *Adv. Mater.*, 2019, **31**, 1805230.

4 J. Li, S. Chen, N. Yang, M. Deng, S. Ibraheem, J. Deng, J. Li, L. Li and Z. Wei, Ultrahigh-loading zinc single-atom catalyst for highly efficient oxygen reduction in both acidic and alkaline media, *Angew. Chem., Int. Ed.*, 2019, **58**, 7035–7039.

5 A. Han, W. Sun, X. Wan, D. Cai, X. Wang, F. Li, J. Shui and D. Wang, Construction of Co_4 atomic clusters to enable Fe–N_4 motifs with highly active and durable oxygen reduction performance, *Angew. Chem., Int. Ed.*, 2023, **62**, e202303185.

6 Z. Miao, S. Li, C. Priest, T. Wang, G. Wu and Q. Li, Effective approaches for designing stable M–N_x/C oxygen-reduction catalysts for proton-exchange-membrane fuel cells, *Adv. Mater.*, 2022, **34**, 2200595.

7 X. Wan, X. Liu, Y. Li, R. Yu, L. Zheng, W. Yan, H. Wang, M. Xu and J. Shui, Fe–N–C electrocatalyst with dense active sites and efficient mass transport for high-performance proton exchange membrane fuel cells, *Nat. Catal.*, 2019, **2**, 259–268.

8 H. Zhang, H.-C. Chen, S. Feizpoor, L. Li, X. Zhang, X. Xu, Z. Zhuang, Z. Li, W. Hu, R. Snyders, D. Wang and C. Wang, Tailoring oxygen reduction reaction kinetics of Fe–N–C catalyst *via* spin manipulation for efficient zinc–air batteries, *Adv. Mater.*, 2024, **36**, 2400523.

9 Z. Yang, Y. Wang, M. Zhu, Z. Li, W. Chen, W. Wei, T. Yuan, Y. Qu, Q. Xu, C. Zhao, X. Wang, P. Li, Y. Li, Y. Wu and Y. Li, Boosting oxygen reduction catalysis with Fe–N_4 sites decorated porous carbons toward fuel cells, *ACS Catal.*, 2019, **9**, 2158–2163.

10 Q. Qu, Y. Mao, S. Ji, J. Liao, J. Dong, L. Wang, Q. Wang, X. Liang, Z. Zhang, J. Yang, H. Li, Y. Zhou, Z. Wang, G. I. N. Waterhouse, D. Wang and Y. Li, Engineering the lewis acidity of fe single-atom sites *via* atomic-level tuning of spatial coordination configuration for enhanced oxygen reduction, *J. Am. Chem. Soc.*, 2025, **147**, 6914–6924.

11 M. Liu, Y. Liu, X. Zhang, L. Li, X. Xue, M. Humayun, H. Yang, L. Sun, M. Bououdina, J. Zeng, D. Wang, R. Snyders, D. Wang, X. Wang and C. Wang, Altering the symmetry of Fe–N–C by axial cl-mediation for high-performance zinc–air batteries, *Angew. Chem., Int. Ed.*, 2025, **64**, e202504923.

12 J. Qiao, C. Lu, L. Kong, J. Zhang, Q. Lin, H. Huang, C. Li, W. He, M. Zhou and Z. Sun, Spin engineering of Fe–N–C by axial ligand modulation for enhanced bifunctional oxygen catalysis, *Adv. Funct. Mater.*, 2024, **34**, 2409794.

13 L. Peng, J. Yang, Y. Yang, F. Qian, Q. Wang, D. Sun-Waterhouse, L. Shang, T. Zhang and G. I. N. Waterhouse, Mesopore-rich Fe–N–C catalyst with FeN_4–O–NC single-atom sites delivers remarkable oxygen reduction reaction performance in alkaline media, *Adv. Mater.*, 2022, **34**, 2202544.

14 X. Wang, Z.-Y. Yi, Y.-Q. Wang and D. Wang, Molecular evidence for the axial coordination effect of atomic iodine on Fe–N_4 sites in oxygen reduction reaction, *Angew. Chem., Int. Ed.*, 2025, **64**, e202413673.

15 K.-M. Zhao, S. Liu, Y.-Y. Li, X. Wei, G. Ye, W. Zhu, Y. Su, J. Wang, H. Liu, Z. He, Z.-Y. Zhou and S.-G. Sun, Insight into the mechanism of axial ligands regulating the catalytic activity of Fe–N_4 sites for oxygen reduction reaction, *Adv. Energy Mater.*, 2022, **12**, 2103588.

16 X.-W. Lv, J. Gong, S. Wang, X. Yan, C. Sun, X. Hu, Z. Lai, Y. Liu, H. Wang, Z.-Y. Yuan and J. Geng, Engineering orbital hybridization in advanced electrocatalysts for energy conversion: fundamentals, modulations, and perspectives, *Adv. Energy Mater.*, 2025, **15**, 2501129.

17 A. Zitolo, V. Goellner, V. Armel, M.-T. Sougrati, T. Mineva, L. Stievano, E. Fonda and F. Jaouen, Identification of catalytic sites for oxygen reduction in iron- and nitrogen-doped graphene materials, *Nat. Mater.*, 2015, **14**, 937–942.

18 L. Wang, L. Yang, X. Zhao, H. Ma, B. Pang, L. Duan, K. Zeng, L. Liu, A. Chen and H. Guo, Using CrN_4 moiety to weaken the dissociation barrier of hydroxyl on adjacent single iron atom for efficient oxygen reduction, *Energy Storage Mater.*, 2025, **74**, 103927.

19 C. Liu, R. Yang, J. Wang, B. Liu, X. Chang, P. Feng, X. Zhang, L. Zhong, X. Zhao, L. Niu, S. Gan, Y. Xi, M. Huang and H. Wang, Synergistic catalysts with Fe single atoms and fe3c clusters for accelerated oxygen adsorption kinetics in oxygen reduction reaction, *Angew. Chem., Int. Ed.*, 2025, **64**, e202501266.

20 S. Zhang, J. Wu, M. Zheng, X. Jin, Z. Shen, Z. Li, Y. Wang, Q. Wang, X. Wang, H. Wei, J. Zhang, P. Wang, S. Zhang, L. Yu, L. Dong, Q. Zhu, H. Zhang and J. Lu, Fe/Cu diatomic catalysts for electrochemical nitrate reduction to ammonia, *Nat. Commun.*, 2023, **14**, 3634.

21 W. Liu, E. Shi, H. Wu, Y. Liang, M. Chen, H. Zhang, R. Zhang, X. Li, Y. Wang and L. Zhang, Spatially axial boron coordinated single-atom nanozymes with boosted multi-enzymatic performances for periodontitis treatment, *Adv. Funct. Mater.*, 2024, **34**, 2403386.

22 Y. Zhou, G. Chen, Q. Wang, D. Wang, X. Tao, T. Zhang, X. Feng and K. Müllen, Fe–N–C electrocatalysts with densely accessible $Fe–N_4$ sites for efficient oxygen reduction reaction, *Adv. Funct. Mater.*, 2021, **31**, 2102420.

23 Y. Tan, J. Fu, T. Luo, K. Liu and M. Liu, Theoretical insights into the selectivity of single-atom Fe–N–C catalysts for electrochemical nox reduction, *J. Am. Chem. Soc.*, 2025, **147**, 4937–4944.

24 P. Yin, T. Yao, Y. Wu, L. Zheng, Y. Lin, W. Liu, H. Ju, J. Zhu, X. Hong, Z. Deng, G. Zhou, S. Wei and Y. Li, Single cobalt atoms with precise N-coordination as superior oxygen reduction reaction catalysts, *Angew. Chem., Int. Ed.*, 2016, **55**, 10800–10805.

25 S. Wu, X. Liu, H. Mao, J. Zhu, G. Zhou, J. Chi, Z. Wu and L. Wang, Unraveling the tandem effect of nitrogen configuration promoting oxygen reduction reaction in alkaline seawater, *Adv. Energy Mater.*, 2024, **14**, 2400183.

26 Y. Hu, S. Niu, Z. Zhang, T. Chao, T. Zhao, G. Yu, F. Zhou, X. Liang, H. Jin, Z. Yang, D. Wang, W. Chen and Y. Li, Axial chlorine engineering of p-block antimony atomic sites boosts oxygen reduction, *J. Am. Chem. Soc.*, 2025, **147**(24), 21231–21240.

27 M. Tong, F. Sun, G. Xing, C. Tian, L. Wang and H. Fu, Potential dominates structural recombination of single atom Mn sites for promoting oxygen reduction reaction, *Angew. Chem., Int. Ed.*, 2023, **62**, e202314933.

28 B. Tang, Q. Ji, X. Zhang, R. Shi, J. Ma, Z. Zhuang, M. Sun, H. Wang, R. Liu, H. Liu, C. Wang, Z. Guo, L. Lu, P. Jiang, D. Wang and W. Yan, Symmetry breaking of FeN_4 moiety *via* edge defects for acidic oxygen reduction reaction, *Angew. Chem., Int. Ed.*, 2025, **64**, e202424135.

29 Y. Dai, B. Liu, Z. Zhang, P. Guo, C. Liu, Y. Zhang, L. Zhao and Z. Wang, Tailoring the d-orbital splitting manner of single atomic sites for enhanced oxygen reduction, *Adv. Mater.*, 2023, **35**, 2210757.

30 F. Wang, R. Zhang, Y. Zhang, Y. Li, J. Zhang, W. Yuan, H. Liu, F. Wang and H. L. Xin, Modulating electronic structure of atomically dispersed nickel sites through boron and nitrogen dual coordination boosts oxygen reduction, *Adv. Funct. Mater.*, 2023, **33**, 2213863.

31 C. Hu, G. Xing, W. Han, Y. Hao, C. Zhang, Y. Zhang, C.-H. Kuo, H.-Y. Chen, F. Hu, L. Li and S. Peng, Inhibiting demetalation of Fe–N–C *via* mn sites for efficient oxygen reduction reaction in zinc–air batteries, *Adv. Mater.*, 2024, **36**, 2405763.

32 J. Zhang, J. Chen, Y. Jing, X. Xu, C. Liu and J. Jia, Fe, Co, N-doped composite as an efficient catalyst for oxygen reduction and oxygen evolution reaction, *Mater. Today Chem.*, 2025, **44**, 102531.

33 X. Wang, S. Zhang, M. Li, Y. Wan, Z. Sun, R. Li, Z. Zhu, H. Wu, Z. Zhao, S. Hu, F. Bu, D. Chao and W. Luo, Tailored design of mesoporous metal organic framework single crystals by kinetics-mediated micelle assembly for efficient asymmetrical single-atom catalysis, *Adv. Mater.*, 2025, **37**, 2500370.

34 H. Niu, L. Huang, Y. Qin, R. Qi, B. Mei, D. Wu, F.-M. Li, B. You, Q. Li, Y. Yao, Z. Wang, T. Yao, S. Ding, W. Guo, Y. Chen, Y. Su, F. Song and B. Y. Xia, Hydrogen peroxide spillover on platinum–iron hybrid electrocatalyst for stable oxygen reduction, *J. Am. Chem. Soc.*, 2024, **146**, 22650–22660.

35 T. Tang, X. Xu, X. Bai, C. Hou, T. Gan, Z. Wang and J. Guan, A triatomic cobalt catalyst for oxygen electrocatalysis, *Angew. Chem., Int. Ed.*, 2025, **64**, e202503019.

36 Y. Zhao, H. Wu, Y. Wang, L. Liu, W. Qin, S. Liu, J. Liu, Y. Qin, D. Zhang, A. Chu, B. Jia, X. Qu and M. Qin, Sulfur coordination engineering of molybdenum single-atom for dual-functional oxygen reduction/evolution catalysis, *Energy Storage Mater.*, 2022, **50**, 186–195.

37 Y. Yang, Y. Kang, H. Zhao, X. Dai, M. Cui, X. Luan, X. Zhang, F. Nie, Z. Ren and W. Song, An interfacial electron transfer on tetrahedral $NiS_2/NiSe_2$ heterocages with dual-phase synergy for efficiently triggering the oxygen evolution reaction, *Small*, 2020, **16**, 1905083.

38 Y. Yan, Z. Ran, T. Zeng, X. Wen, H. Xu, R. Li, C. Zhao and C. Shu, Interfacial electron redistribution of hydrangea-like Nio@Ni_2p heterogeneous microspheres with dual-phase synergy for high-performance lithium–oxygen battery, *Small*, 2022, **18**, 2106707.

39 J.-Y. Yue, Z.-X. Pan, Y. Guo, P. Yang and B. Tang, Distinct oxygen reduction pathways for solar H_2O_2 production by regulating unsaturated bonds in covalent organic frameworks, *Chem. Sci.*, 2025, **16**, 13883–13892.

40 Z. Li, S. Ji, C. Xu, L. Leng, H. Liu, J. H. Horton, L. Du, J. Gao, C. He, X. Qi, Q. Xu and J. Zhu, Engineering the electronic structure of single-atom iron sites with boosted oxygen bifunctional activity for zinc–air batteries, *Adv. Mater.*, 2023, **35**, 2209644.

41 X. Wang, J. Wang, P. Wang, L. Li, X. Zhang, D. Sun, Y. Li, Y. Tang, Y. Wang and G. Fu, Engineering 3d–2p–4f gradient orbital coupling to enhance electrocatalytic oxygen reduction, *Adv. Mater.*, 2022, **34**, 2206540.

42 J.-H. Zheng, G. Li, J.-M. Zhang, N. Cheng, L.-F. Ji, J. Yang, J. Zhang, B.-W. Zhang, Y.-X. Jiang and S.-G. Sun, General strategy for evaluating the d-band center shift and ethanol oxidation reaction pathway towards pt-based electrocatalysts, *Sci. China: Chem.*, 2023, **66**, 279–288.

43 L. Yang, R. Grzeschik, S. Schlücker and W. Xie, Contact electrification as an emerging strategy for controlling the performance of metal nanoparticle catalysts, *Chem.–Eur. J.*, 2024, **30**, e202401718.

44 R. Cheng, X. He, M. Jiang, X. Shao, W. Tang, B. Ran, H. Li and C. Fu, F–p–d gradient orbital coupling induced spin state enhancement of atomic fe sites for efficient and stable oxygen reduction reaction, *Adv. Funct. Mater.*, 2025, **35**, 2425138.

45 Z. Li, Z. Zhuang, F. Lv, H. Zhu, L. Zhou, M. Luo, J. Zhu, Z. Lang, S. Feng, W. Chen, L. Mai and S. Guo, The marriage of the fen4 moiety and mxene boosts oxygen reduction catalysis: Fe 3d electron delocalization matters, *Adv. Mater.*, 2018, **30**, 1803220.

46 Y. Zhou, K. Yin, Y. Huang, J. Li, A. Zhu, D. Lin, G. Gan, J. Zhang, K. Liu, T. Zhang, K. Liu, C. Luan, H. Yang, H. Chen, S. Guo, W. Zhang and G. Hong, D-orbital reconstruction achieves low charge overpotential in li-oxygen batteries, *Nat. Commun.*, 2025, **16**, 3353.

47 Z. Han, S. Zhao, J. Xiao, X. Zhong, J. Sheng, W. Lv, Q. Zhang, G. Zhou and H.-M. Cheng, Engineering d–p orbital hybridization in single-atom metal-embedded three-dimensional electrodes for li–s batteries, *Adv. Mater.*, 2021, **33**, 2105947.

48 H. Cai, S. He, H. Yang, Q. Huang, F. Luo, Q. Hu, X. Zhang and C. He, Highly exposed ultra-small high-entropy sulfides with d–p orbital hybridization for efficient oxygen evolution, *Adv. Mater.*, 2025, **37**, 2508610.

49 M. Tamtaji, Q. Peng, T. Liu, X. Zhao, Z. Xu, P. R. Galligan, M. D. Hossain, Z. Liu, H. Wong, H. Liu, K. Amine, Y. Zhu, W. A. Goddard Iii, W. Wu and Z. Luo, Non-bonding interaction of dual atom catalysts for enhanced oxygen reduction reaction, *Nano Energy*, 2023, **108**, 108218.

50 H. Long, X. Zhang, Z. Zhang, J. Zhang, J. Yu and H. Yu, Fine-tuning d–p hybridization in Ni–B_x cocatalyst for enhanced photocatalytic H_2 production, *Nat. Commun.*, 2025, **16**, 946.

51 B. Jing, Q. Zhang, M. Liu, S. Yang, J. Zhang, S. Qiu, I. Sirés and F. Deng, Magnetically-altered e_g-orbital occupancy to boost the two-electron oxygen reduction electrocatalysis for faster water decontamination, *Appl. Catal., B*, 2025, **369**, 125149.

52 X. Yue, L. Cheng, E. Baráth, R. V. Jagadeesh and Q. Xiang, Deciphering orbital hybridization in heterogeneous catalysis, *Electron*, 2024, **2**, e16.

53 Y. Qi, K. Song, Q. Liang, X. Zhou, M. Liu, W. Li, F. Liu, Z. Jiang, Q. Gu, Z. Chen, B. Zhang and W. Zhang, Asymmetric b-coordination stimulated high-spin cobalt boosts orr, *Nano Res.*, 2025, **18**, 94907278.

54 X. Wang, J. Zhang, P. Wang, L. Li, H. Wang, D. Sun, Y. Li, Y. Tang, X. F. Lu, Y. Wang and G. Fu, Terbium-induced cobalt valence-band narrowing boosts electrocatalytic oxygen reduction, *Energy Environ. Sci.*, 2023, **16**, 5500–5512.

55 S. Ning, M. Li, X. Wang, D. Zhang, B. Zhang, C. Wang, D. Sun, Y. Tang, H. Li, K. Sun and G. Fu, Importing antibonding-orbital occupancy through Pd–O–Gd bridge promotes electrocatalytic oxygen reduction, *Angew. Chem., Int. Ed.*, 2023, **62**, e202314565.

56 X. Zhong, Z. Zheng, J. Xu, X. Xiao, C. Sun, M. Zhang, J. Ma, B. Xu, K. Yu, X. Zhang, H.-M. Cheng and G. Zhou, Flexible zinc–air batteries with ampere-hour capacities and wide-temperature adaptabilities, *Adv. Mater.*, 2023, **35**, 2209980.